Impact of Warhead Modulations on the Covalent Inhibition of SARS-CoV-2 Mpro Explored by QM/MM Simulations

# Impact of Warhead Modulations on the Covalent Inhibition of SARS-CoV-2 $M^{pro}$ Explored by QM/MM Simulations

Sergio Martí,[1] Kemel Arafet,[1,2] Alessio Lodola,[2] Adrian J. Mulholland,[3] Katarzyna Świderek,[1,*] Vicent Moliner.[1,*]

1. BioComp Group, Institute of Advanced Materials (INAM), Universitat Jaume I, 12071 Castelló, Spain.
2. Dipartimento di Scienze degli Alimenti e del Farmaco, Università degli Studi di Parma, I-43124 Parma, Italy.
3. Centre for Computational Chemistry, School of Chemistry, University of Bristol, Bristol BS8 1TS, United Kingdom.

**Keywords:** SARS-CoV-2 $M^{pro}$, COVID-19, inhibition, methyl oxo-enoate based inhibitors, ketone-based Michael acceptor inhibitors, QM/MM, MD.

**Corresponding Authors**

* K. Ś., E-mail: swiderek@uji.es
* V. M., E-mail: moliner@uji.es

**ABSTRACT**

The COVID-19 pandemic, caused by the severe acute respiratory syndrome coronavirus-2, SARS-CoV-2, shows the need for effective antiviral treatments. Here, we present a simulation study of the inhibition of the SARS-CoV-2 main protease ($M^{pro}$), a cysteine hydrolase essential for the life cycle of the virus. The free energy landscape for the mechanism of the inhibition process is explored by QM/MM umbrella sampling and free energy perturbation simulations at the M06-2X/MM level of theory for two proposed peptidyl covalent inhibitors that share the same recognition motif but feature distinct cysteine-targeting warheads. Regardless of intrinsic reactivity of the modelled inhibitors, namely a Michael acceptor and a hydroxymethylketone activated carbonyl, our results confirm that the inhibitory process takes place by means of a two-step mechanism, in which the formation of an ion pair C145/H41 dyad precedes the protein-inhibitor covalent bond formation. The nature of this second step is strongly dependent on the functional groups in the warhead: while the nucleophilic attack of the C145 sulfur atom on the Cα of the double bond of the Michael acceptor takes place concertedly with the proton transfer from H41 to $C_\beta$, in the compound with an activated carbonyl, the sulfur attacks the carbonyl carbon concomitant with the proton transfer from H41 to the carbonyl oxygen through the hydroxyl group. Analysis of the free energy profiles, structures along the reaction path, and interactions between the inhibitors and the different pockets of the active site on the protein shows a measurable impact of the warhead on the kinetics and thermodynamics of the process. These results, and QM/MM methods, can be used as a guide to select warheads to design efficient irreversible and reversible inhibitors of SARS-CoV-2 $M^{pro}$.

## INTRODUCTION

Despite the development of efficient vaccines, the impact of the COVID-19 pandemic around the world, produced by the severe acute respiratory syndrome coronavirus-2 – SARS-CoV-2 – has emphasized the need for antiviral treatments. Moreover, considering the capabilities of the virus to mutate, like any other viruses that contain RNA genetic material such as this or the influenza viruses, the corresponding risk of a decrease in the effectiveness of the vaccines urged the need for complementary strategies to fight against the pandemic. Many efforts have focused on understanding the life cycle of SARS-CoV-2, to provide information about possible ways of developing drugs.[1-3] Among the proteins involved in the replication of the virus, the main coronavirus protease (SARS-CoV-2 $M^{pro}$) is a most attractive target due to its intrinsic features, including its distinguishing ability to cleave proteins after glutamine residue,[4] catalytic features which make $M^{pro}$ unique with respect to human proteases. The most effective $M^{pro}$ inhibitors so far identified, including the clinical candidates PF-00835231, incorporate a glutamine residue or a bioisostere at P1 position (see below) to give potency and selectivity, and a peptidomimetic scaffold of moderate size endowed with branched hydrophobic substituents at both P2 and P3 positions.[5-7] These compounds act by a covalent mechanism, so a reactive 'warhead' is required, i.e. an electrophilic group to form the covalent bond formation between the active site cysteine residue (C145), previously activated by a histidine residue (H41), and the inhibitor. Warheads that have been traditionally used in cysteine proteases range from classical Michael acceptors (MAs) to activated carbonyl derivatives, including alpha-ketoamides, aldehydes and hydroxymethylketone (HMK).[4,6,8] Nevertheless, the previous investigation on $M^{pro}$ inhibition by those prototypical warheads does not assess their relative reactivity versus C145, nor explore the contribution played by the recognition part to the overall inhibition process.

Thus, there is an urgent need to understand the effects of warheads on reactivity as well as on the chemical stability of the covalent adduct generated. This second aspect is fundamental in the context of drug development as it affects the (ir)reversibility of inhibition. Irreversible inhibition through a covalent mechanism is generally the most effective strategy to obtain a sustained response *in vivo* since release from inhibition requires the resynthesis of the engaged target. However, it can challenging to identify covalent compounds that selectively react with the specific residue without causing irreversible labelling of other (host) targets that may lead to liver toxicity and/or immune

responses. These concerns about off-target modifications are motivating the search for potent covalent and reversible agents. It is also important to be able to explore a range of different pharmacokinetic behavior, and in particular, there is a need to predict the degree of reversibility of inhibition. It is therefore critical to develop computational protocols able to predict the kinetic behavior of a covalent inhibitor.

A plethora of different computational methods has been used since the emergence of COVID-19 for the discovery of small-molecule therapeutics.[7,9] Regarding the inhibition of $M^{pro}$, modelling based on classical force fields can contribute to the discovery and optimization of noncovalent inhibitors,[10-12] while the use of methods based on quantum mechanics/molecular mechanics (QM/MM) potentials can assist the design of covalent inhibitors. We recently studied the mechanism of the covalent inhibition by the peptidyl-MA compound **N3** designed by Jin and colleagues,[6] and by two designed MA compounds (**B1** and **B2**) by QM/MM molecular dynamics (MD) methods.[13] Our results indicated that both designed compounds may be promising candidates as drug leads against COVID-19. Interestingly, according to the computed thermodynamic properties of the full inhibition process, **B1** could behave as an irreversible inhibitor while **B2** and may be a reversible inhibitor. The reaction free energies of the inactivation of $M^{pro}$ with **B1** and **B2** were–27.9 and –11.4 kcal·mol$^{-1}$, respectively.

As previously proposed from structures from X-ray diffraction studies,[3] and later supported by computational studies using several different approaches, the chemical reaction step of the $M^{pro}$ inactivation involves the activation of the SH group of C145 by the imidazole group of H41. Then, the formed reactive nucleophilic thiolate ($CysS^-$) would attack the inhibitor making the inhibitor-protein covalent bond.[13-18] According to the recent literature, the equilibrium between the neutral dyad and the $CysS^-/HisH^+$ ion pair appears to be tipped in favour of the neutral pair by ligand binding, but this may depend on the stereoelectronic properties of the ligand itself. Thus, while some simulation studies report a neutral dyad significantly more stable than the ion pair (by ca. 11 kcal·mol$^{-1}$) or identifying the ion pair as a not stable state,[18] others suggest the ion pair is not so destabilized with respect to the initial neutral dyad,[13,14] or is even slightly more stable than the neutral dyad (e.g. our previous study with **B1**).[13]

Our previous study on the proteolysis reaction of SARS-CoV-2 $M^{pro}$, using a polypeptide with a fluorescent 7-amino-4-carbamoylmethylcoumarin tag, concluded that this enzyme somewhat differs from other cysteine proteases, from the mechanistic point of view.[15] Thus, the initial enzyme:substrate complex would not be the ion pair dyad $C145^-/H41^+$

(**E**$^{(+/-)}$**:I**) but rather the neutral C145/H41 dyad (**E:I**). This result is in agreement with studies carried out by us, and others, using different inhibitors and substrates,[13,16,18] but in contrast with the protonation state of the catalytic dyad suggested from the ligand-free SARS–CoV-2 M$^{pro}$ recently solved by neutron crystallography at pH 6.6.[19] Nevertheless, as already pointed out, questions remain about how pH or the presence of an inhibitor or substrate influence the protonation state of the dyad in SARS-CoV-2 M$^{pro}$.[16] Continuing with the main results of our previous study, in fact the formation of the ion pair dyad C145$^{-}$/H41$^{+}$ (**E**$^{(+/-)}$**:I**) and the nucleophilic attack of sulfur atom of C145 to the carbonyl carbon atom of the peptide take place concertedly. Then, the acylation reaction is completed by the peptide bond breaking which assisted by a proton transfer from the protonated H41$^{+}$ to the substrate, forming a stable acyl-enzyme covalent intermediate.[15] In contrast, in the inhibition reaction by **N3**, or our designed **B1** and **B2** MA compounds,[13] or the simulation with M$^{pro}$-substrate peptide models,[16] the reaction appears to proceed in a stepwise manner. The rate-limiting step of the process, in all these three cases, was the enzyme-inhibitor covalent bond formation, with activation free energies ranging from 11.8 to 9.8 kcal·mol$^{-1}$.[13] Analysis of the QM-MM interaction energies between the substrate (the peptide in the proteolysis reaction or the inhibitor in the case of the inhibitors) and the different binding pockets of M$^{pro}$ and the peptide (in the study of the proteolysis reaction) or the inhibitor (in the case of the inhibitors) confirms that they are dominated by those in the P1:::S1 site. Thus, our previous results indicate that a low barrier C145 covalent modification depends on either the warhead or the recognition portion. The recognition portion dictates how the inhibitor is accommodated in the active site which, in turn affects the subsequent chemical reaction step. Consequently, to design an efficient inhibitor must take into account the reactivity of the warhead and the favorable interactions between the recognition portion and the active site of the enzyme.[20] In all, the experience accumulated based on the results derived from previous studies on this and other cysteine proteases can be used to guide the design of new compounds, and QM/MM simulations can be considered a useful tool to get a detailed description of the chemical steps of the inhibition of protein targets covalent inhibitors. Moreover, the obtained activation free energies and the reaction energies obtained with these high level methods can confirm, or not, the viability of the proposed inhibitors.

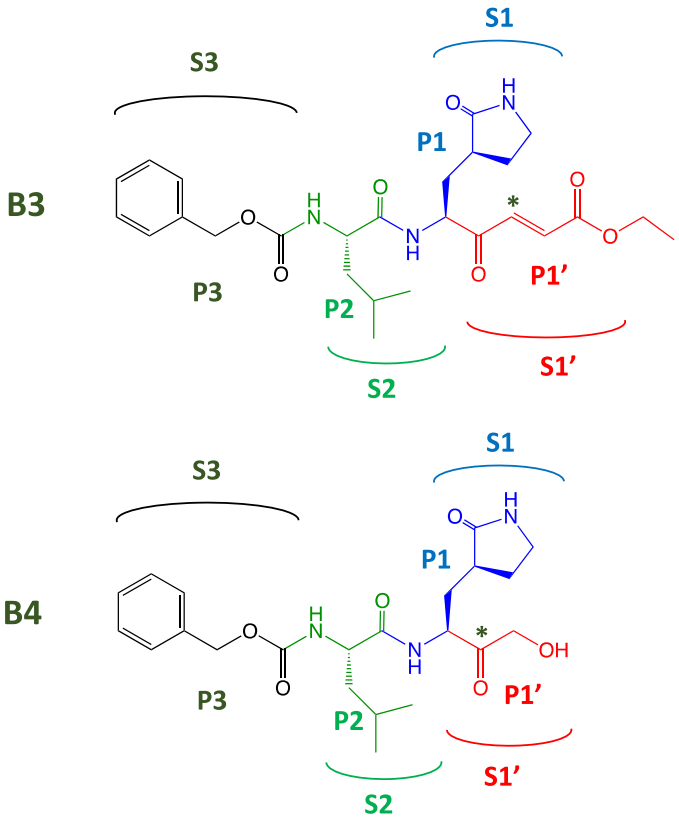


**Scheme 1**. Chemical structures of the proposed (**B3** and **B4**) inhibitors of SARS-CoV-2 $M^{pro}$. The warheads, P1', are highlighted in red, while P1, P2 and P3 fragments are in blue, green and black, respectively. The subpockets of the active site are labeled with S numbering complementary to fragments of the inhibitor. Asterisks indicate the main reactive centre of the inhibitors.

Here, we propose and investigate the inhibition of the SARS-CoV-2 $M^{pro}$ by two potential covalent (peptidyl) inhibitors endowed with two chemically diverse warheads. Building upon the findings on information derived from our previous studies on the proteolysis of $M^{pro}$,[15] and on the reaction of the inhibition with several peptidyl irreversible inhibitors,[13] two compounds **B3** and **B4** are proposed (Scheme 1). A methyl oxo-enoate was used in **B3,** inspired by dimethylfumarate structure,[21,22] while a hydroxymethylketone (HMK) was used as a warhead in the **B4** compound. This reactive group is also present in the structure of PF-00835231 $M^{pro}$ inhibitor, now being under a clinical trial[5]. The recognition part possessed by both B3 and B4 compounds was selected based on QM/MM results obtained with previously proposed inhibitors **B1** and **B2**, and from analysis of protein-substrate interactions from QM/MM simulation of the proteolysis reaction.[15] We keep the recognition part as a short peptide-like compound, combining the P1 moiety of **B1** and the P2 and P3 moiety of **B2**. This is a robust and systematic way of deciphering the effect of specific changes in the intrinsic chemical reactivity of the proposed inhibitors on the

mechanism (and energetics) of inhibition. As shown in our previous studies, stabilizing ligand:protein interactions were established when using this relatively small recognition part.[13] Thus, S2 is a small hydrophobic pocket without strong hydrogen bond interactions with P2. Therefore, an isobutyl group was kept at the P2 site as in **B2**. The S3 subsite of $M^{pro}$ is completely exposed to the solvent and then we keep the shorter P3 of **B2**. Also, previous studies[6] suggest that different kind of substituents can be used in P3. It must be kept in mind that despite the fact that the PF-00835231 $M^{pro}$ inhibitor shows an interaction between the indole group (removed in our new compounds) and E166, our previous study revealed favorable interactions between P3 and M165 and Q189.[13] Finally, the glutamine present in P1 of **B1** was employed in these new compounds due to the favorable interactions observed in our previous study of the proteolysis.[15]

From a mechanistic point of view, the two proposed compounds could potentially react in different manners in the active site of the enzyme, also because their key electrophilic centers not only possess a different chemical environment but they are not topologically equivalent. Thus, as shown in Scheme 2, after the formation of the ion pair **$E^{(+/-)}$:I** reactant complex with **B3**, the attack of the sulfur of C145 to the β-carbon of the substrate can take place, followed by the proton transfer from the protonated H41 to the α-carbon, leading to a stable covalent product **E-I**. Nevertheless, considering the nature of the warhead in **B3**, the final proton transfer could also take place to the carbonyl oxygen atom (**E-I'**). In the case of the inhibition with **B4**, this dual possibility of the final proton transfer does not appear after the acylation of the enzyme because the proton from H41 can only be transferred to the carbonyl oxygen atom of the inhibitor (Scheme 3).

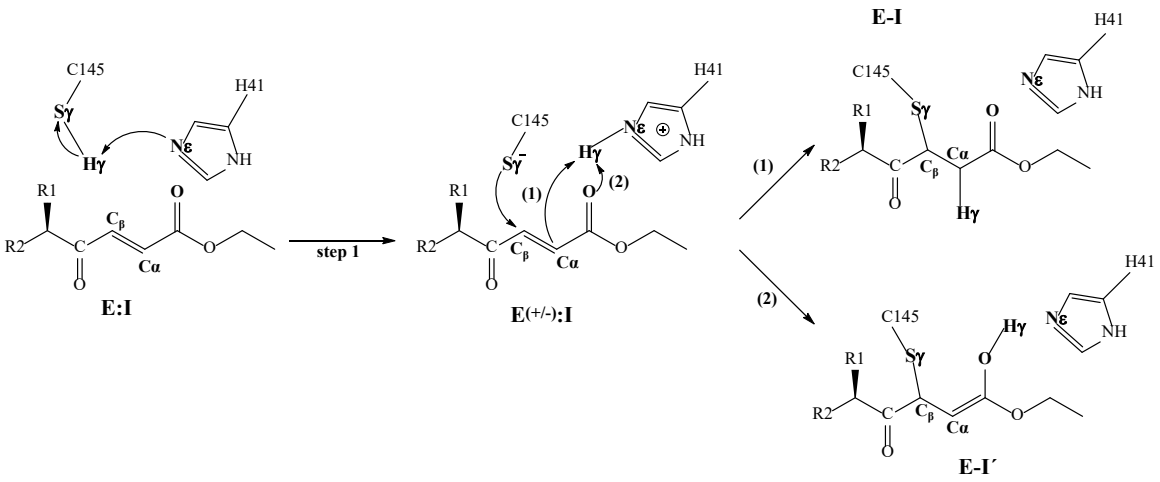


**Scheme 2.** Proposed mechanism of SARS-CoV-2 $M^{pro}$ cysteine protease inhibition by **B3**. R1 and R2 are the different substituents, as shown in Scheme 1.

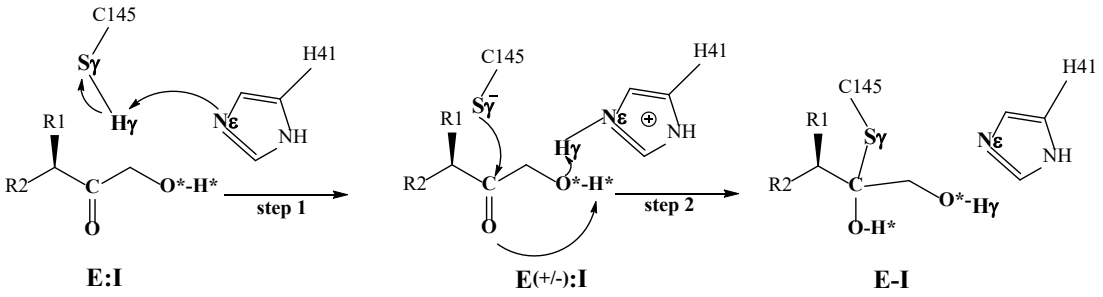


**Scheme 3.** Proposed mechanism of SARS-CoV-2 $M^{pro}$ cysteine protease inhibition by **B4**. R1 and R2 are different substituents, as shown in Scheme 1.

The present study is a computational study of the mechanism of inhibition of $M^{pro}$ by **B3** and **B4**. The reaction mechanisms for each inhibitor were initially explored by nudged elastic band calculation of the minimum energy paths. Then, two free energy-based methodologies, such as the umbrella sampling (US) and free energy perturbation (FEP) methods, both at density functional theory level combined with classical force fields, were employed to explore the full inhibition process.

## COMPUTATIONAL METHODS

The coordinates for the starting point were taken from the X-Ray structure of the SARS-CoV-2 $M^{pro}$ complexed with the PF-00835231 inhibitor (PDB ID 6XHM).[5] The PF-00835231 inhibitor was then manually modified leading to the two new enzyme-inhibitor models. The missing force field parameters for each model were generated using the Antechamber program,[23] available in the AmberTools package (see Table S1 and S2 of Supporting Information). The protonation states of the titratable amino acids were determined using the empirical program PropKa ver. 3.0.3,[24] while the histidine residues were assigned by detailed visual inspection. According to the results, all titratable residues were protonated in their standard state in an aqueous solution at pH 7 (see a list of all the pKa values in Table S3 of Supporting Information). Each model was neutralized by adding 8 sodium counter ions that were placed in a box of 92.154 × 102.242 × 97.285 $Å^3$ of TIP3P[25] water molecules.

The next step for each model consisted of $10^5$ steps of conjugate-gradient minimization, followed by a series of molecular dynamics (MD) simulations in the NVT ensemble with the AMBER ff03 force field,[26] as implemented in NAMD software:[27] 100 ps of MD was performed for heating up to 310 K, followed by 10 ns of equilibration, using the Langevin

thermostat.[28] All simulations made use of the PME algorithm for the electrostatic interactions with a force-switch scheme ranging from 14.5 to 16 Å, and a time step of 1 fs. Analysis of the time evolution of the root-mean-square deviations of the backbone atoms of the protein models, using the cpptraj facility,[29] confirmed that the two models become equilibrated (see Figures S1a and S2a of the Supporting Information).

In this work, an additive hybrid QM/MM scheme was selected for constructing the total Hamiltonian. The QM subset of atoms includes the P1', P1 and P2 positions of the inhibitor, together with C145 and H41 residues of the protein. Four link atoms were inserted where the QM/MM boundary intersected covalent bonds in the positions indicated on Figures S1b and S2b in the Supporting Information. Thus, the QM part consisted of 89 atoms for the inhibitor **B3** and 80 for the **B4**.

All the calculations were performed with the QMCube suite,[30] for which the combination of the NAMD and Gaussian09[31] programs was used for constructing the potential energy function. The AMBER ff03[26] and the TIP3P[25] force fields were selected to describe the MM atoms, and the Minnesota functional M06-2X[32] with the split-valence 6-31+G(d,p) basis set[33] were used to treat the QM subset of atoms. This functional has been tested and shown to be suitable for modelling this type of reactivity.[13,15,16,34,35] The position of any atom over 25 Å from the substrate was fixed to speed up the calculations.

Reaction mechanisms for each inhibitor were initially explored using the nudged elastic band (NEB)[36] approach to set up plausible starting geometries for the transition structures. Then, they were localized and characterized by a micro-macro[37,38] Hessian-based localization scheme, and minimum energy paths (MEP) were traced towards the corresponding minima. The information obtained in this stage was used in the fine-tuning of the free energy methodologies, specifically the potential of mean force (PMF) and free energy perturbation (FEP) methods. We applied these two distinct approaches separately to calculate the free energy profiles for the reaction. It is important to point out that herein we directly compute the free energy landscape at a higher DFT/MM level than in our previous QM/MM studies on the inhibition of $M^{pro}$. Thus, the present calculations apply a significantly higher level of theory in sampling, as detailed below.

In the case of the FEP method, which has been successfully employed in our laboratory for reactivity studies in various biological systems,[39-42] the reaction path obtained for each of the mechanisms was analyzed to extract those consecutive geometries with a cumulative energy difference greater than or equal to 1.5 $kJ \cdot mol^{-1}$ (called 'windows'). Then, pure MM MD simulations were performed on each of these windows, keeping

frozen the atoms of the QM part. Each MD run was performed in the NVT ensemble with a time step of 1 fs and a total time length of 20 ps. The partial charges of the QM atoms were recalculated every 200 steps using the CHELPG[43] methodology, because the MM region is changing during the sampling at every window and can polarize the QM wave function, and consequently propagate to the MM engine (NAMD). The application of this protocol resulted in a total number of 100 structures per window (called "points") with the same coordinates for the QM atoms, but with a different MM environment configuration. In the following step, the coordinates of the QM atoms for each point of the *ith* window were replaced by those of the consecutive window (i+1), and both the perturbed QM and Lennard-Jones energy terms were evaluated. The free energy of the chemical step is then obtained from the cumulative sum of the free energy differences between successive windows, as shown in equation 1:

$$\Delta F_{i\rightarrow i+1} \approx -RTln\left\langle e^{-\frac{U_{i+1}-U_i}{k_BT}}\right\rangle_i \quad (1)$$

where both $U_i$ and $U_{i+1}$ comprise the first three terms of equation 1 (that is: $E_{QM}$, $E_{QM/MM}^{elect}$ and $E_{QM/MM}^{vdW}$), and the average is carried out on all points of the *ith* window. Finally, the free energy profile is obtained from the FEP method, including the corresponding QM zero-point energy (ZPE) for the stationary points.

The potential of mean force for each chemical step was obtained using the combination of the umbrella sampling (US) approach[44] combined with the weighted histogram analysis method (WHAM).[45] Series of MD simulations were performed adding a restraint along the collective reaction coordinate *s*,[46] with an umbrella force constant of 3000 kJ·mol$^{-1}$·Å$^{-2}$. In every window, QM/MM MD-NVT simulations were performed with a total of 3.25 ps at 310 K with a time step of 0.5 fs (a total of 6500 steps). The definition of the *s* coordinate depended on the considered step, always reduced to a combination of distances. Thus for the first step of the inhibitor **B3**, the following distances were included: d(Sγ, Cβ), d(Sγ, Hγ), and d(Hγ, Nε). In the second step, only the protonation of the double bond was studied because the protonation of the carbonyl group gave a high barrier in FEP calculations; therefore, the distances involved were d(Sγ, Cβ), d(Hγ, Cα), and d(Hγ, Nε). In the case of the **B4** inhibitor, the distance d(H*, O) was also accounted for in the first step, being the carbon of the carbonyl moiety the one involved. The second step was followed with the combination of the distances: d(Sγ, C), d(Hγ, Nε), d(Hγ, O*), d(H*, O*), and d(H*, O). All the information needed to define the equally distributed milestones from which the collective variable *s* is constructed were obtained from the

analysis of the different MEPs previously traced. In addition, the error of the PMFs was evaluated as the standard deviation derived from a total of 1000 randomly bootstrapped PMFs.[47]

Finally, the interaction energy was computed as a contribution of each residue of the protein to the interaction energy with the QM part of the substrate was computed using the following expression:

$$E_{QM/MM}^{Int} = \sum \left\langle \Psi \left| \frac{q_{MM}}{r_{e,MM}} \right| \Psi \right\rangle + \sum \sum \frac{Z_{QM} q_{MM}}{r_{QM,MM}} + E_{QM/MM}^{vdW} \quad (2)$$

This interaction energy can be exactly decomposed in a sum over residues provided that the polarized wave function (Ψ) is employed to evaluate this energy contribution. Because of the large number of structures that must be evaluated to obtain a representative population, the QM atoms were described by the semiempirical Hamiltonian AM1[48] in these QM/MM MD calculations.

## RESULTS AND DISCUSSION

The first step in our study was to carry out a deep analysis of the interactions established between the two studied compounds and the active site of $M^{pro}$ in the initial **E:I** state. Figure 1 shows a schematic representation of hydrogen bond interactions, while Figure 2 reports the average interaction energies (electrostatic plus Lennard-Jones) between $M^{pro}$ residues and inhibitor fragments, thus including some interactions with residues that are not necessary at a close distance from the inhibitor. A list of relevant interatomic distances is deposited in Table S4 and S5 of the Supporting Information. Analysis of the results confirms the formation of a stable reactant Michaelis complex in both cases, with a similar pattern of interactions. Keeping in mind that the difference between **B3** and **B4** is restricted to the warhead, and in both cases the interactions with the S1' take place through mainly hydrogen bond interactions with the carbonyl oxygen next to P1 that is common in both inhibitors, the results appear as reasonable despite the very different functional groups in the P1' position. Thus, this carbonyl group is interacting with the oxyanion hole located in S1' formed by G143, S144, and C145. In addition, some not direct interactions that also stabilize the P1' fragment, such as L27, N28, G146 and S147 were identified. The specific favorable interactions between the lactam ring on P1 and S1 are almost equivalent in both inhibitors, mainly through interactions with P140, N142, H163 and E166 (see Figure 2). The backbone atoms of the residues of the P2 site are responsible for the interactions with Q189, H164, D187 and M165. Finally, it is worth

mentioning the unfavorable interaction between R40 and the warhead of B3 and B4. Interestingly, R40 is ca. 8 Å from P1' and the interaction, established basically between the carbonyl group of the peptide bond of R40 and the P1', corresponds to electrostatic interaction. Thus, possible strategies to avoid this interaction in future inhibitor designs would require the redesign of the warheads. There are other positively charged side chains around the inhibitors at similar distances, such as K61 and R188, but their contribution is much less than R40, especially in the case of **B4**, due to a more solvent exposure (see Figure 2 and Figure S3 in the Supporting Information). The conformation adopted by both compounds in the active site of $M^{pro}$ can be compared with the X-ray crystal structures of related complexes. Thus, the cocrystal structure of the covalent adduct of PF-00835231 bound to SARS-CoV-2 $M^{pro}$ (PDB code 6XHM)[5] that, as commented above is like **B4**, shows protein-ligand distances in S1, S2 and S3 equivalent to the ones shown in Figure 1b. These similarities are also observed when comparing the distances between the key atoms involved in the inhibition reaction, $S\gamma^{C145}$ – $C^{C=O}$, $S\gamma^{C145}$ – $N\varepsilon^{H41}$ and $N\varepsilon^{H41}$ – $O^{*OH}$: 1.86, 3.71 and 3.80 Å, respectively, in the crystal structure, and 2.90, 3.13 and 2.34 Å, respectively, in the **B4** complex. Regarding the **B3**, despite no X-ray structure is available for SARS-CoV-2 $M^{pro}$ complexed with a structure comparable to **B3**, there is a cocrystal structure of the covalent adduct 2 of Hoffman and co-workers bound to SARS-CoV-1 $M^{pro}$ (PDB code 6XHO).[5] Analysis of this structure provides similar conclusions regarding the interactions between the different sub-sites of the active site of the related proteins, CoV-1 and CoV-2 $M^{pro}$, and the corresponding compounds in the X-ray structure of SARS-CoV-1 $M^{pro}$ and **B3** in SARS-CoV-2 $M^{pro}$. Obviously, the absence of the carbonyl group at $\alpha$ position of P1' in **2** explains the lack of interactions with the oxyanion hole of the S1' site. Nevertheless, the comparison of the inter-atomic distances that are related with the inhibition reaction, $S\gamma^{C145}$ – $C_\beta$, $S\gamma^{C145}$ – $N\varepsilon^{H41}$, and $N\varepsilon^{H41}$ – $C\alpha$, also shows similar values: 1.76, 3.96 and 3.23 Å, respectively, in the crystal structure, and 3.29, 3.29 and 4.09 Å, respectively, in **B3**. Obviously, this comparison must be done with caution because the X-ray structures correspond to the protein-inhibitor covalent complex (**E-I** in our schemes 2 and 3) while the **B3** and **B4** structures analyzed at this point correspond to the initial reactant complex **E:I**. Thus, differences observed in the distances defining the attack of the sulfur atom of C145 to the corresponding carbon atom of the inhibitor ($C^{C=O}$ or $C_\beta$ for **B3** and **B4**, respectively) are as expected. Anyway, the good overlapping of the X-ray structures and the equilibrated **E:I** reactant complex

support the quality of our initial state structures (see Figures S4 and S5 in the Supporting Information).

Once confirmed that the **E:I** complex represents a stable reactant complex, in both cases, the inhibition reaction was studied according to the general mechanisms proposed in Scheme 2 and 3 for the reaction with **B3** and **B4**, respectively.

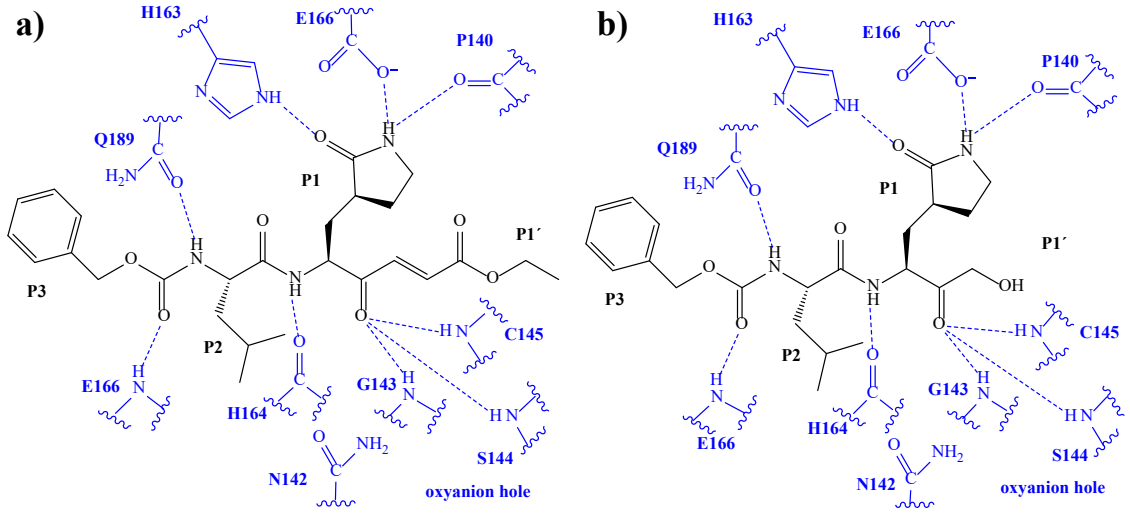


**Figure 1.** Details of the H-bond interactions between the inhibitor and the active site of the SARS-CoV-2 $M^{pro}$ from QM/MM MD simulations of **B3** (a) and **B4** (b) inhibitors in the **E:I** state.

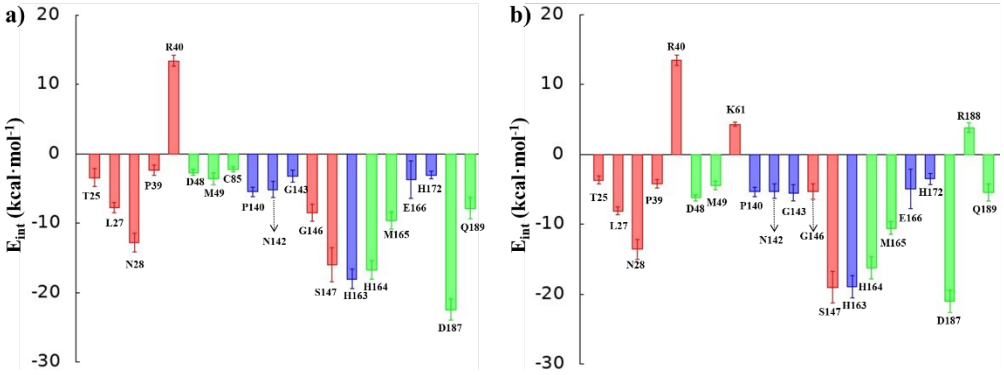


**Figure 2**. Main average interaction energies (electrostatic plus Lennard-Jones) between residues of Chain-A and each fragment of the inhibitor **B3** (a) and **B4** (b) computed at **E:I** state. Results were obtained as an average over 1000 structures from the AM1/MM MD simulations. The red bars correspond to the P1`:::S1` interactions, the blue bars correspond to the P1:::S1 interactions, and the green bars correspond to the P2:::S2 interactions.

## Inhibition of SARS-CoV-2 $M^{pro}$ with B3

As shown in Scheme 2, after the C145 is activated by a proton transfer to H41, thus forming the ion pair complex **E$^{(+/-)}$:I**, the covalent complex is formed by the nucleophilic attack of the sulfur atom of C145 to the $C_\beta$ atom of the **B3** inhibitor. Then, the reaction is completed by the transfer of the proton from the protonated H41 to either the $C_\alpha$ atom, to render the **E-I** final covalent adduct, or to the carbonyl oxygen atom then ending in **E-I'**. Exploration of both mechanisms by M06-2X/6-31+G(d,p)/MM FEP calculations revealed that the formation of the former (i.e. the *direct addition* mechanism) is both thermodynamically and kinetically favored with respect to the formation of **E-I'** (see Figure S6 in Supporting information). Thus, while the reaction that renders the **E-I** product is strongly exergonic (–16.2 kcal·mol$^{-1}$), the energy of **E-I'** product appears to be 15.2 kcal·mol$^{-1}$ higher than the initial reactants state, **E:I**. These differences in the reaction energies are also associated, as mentioned, with significant differences in activation energies; 13.7 and 21.0 kcal·mol$^{-1}$ to form **E-I** and **E-I'**, respectively. Consequently, the much more computationally demanding M06-2X/6-31+G(d,p)/MM US method was applied only to the exploration of the mechanism rendering the **E-I** final product. The resulting free energy profile for the covalent inhibition of SARS-CoV-2 M$^{pro}$ with **B3** is depicted in Figure 3, while the evolution of the selected bond distances along the PMF is shown in Figure 4. Details of the M06-2X/6-31+G(d,p)/MM FESs obtained by means of the US method are given in Figure S7 of the Supporting Information.

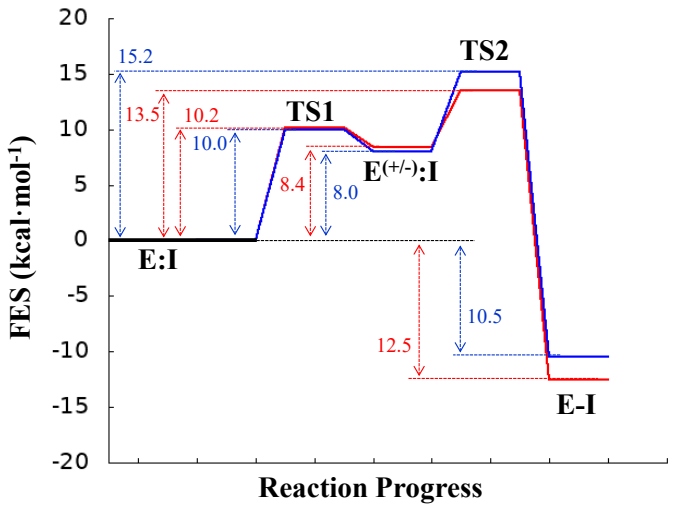


**Figure 3.** M06-2X/6-31+G(d,p)/MM free energy profiles obtained with umbrella sampling MD for the inhibition mechanism of SARS-CoV-2 M$^{pro}$ cysteine protease by **B3** (red line) and **B4** (blue line) inhibitors at 310 K.

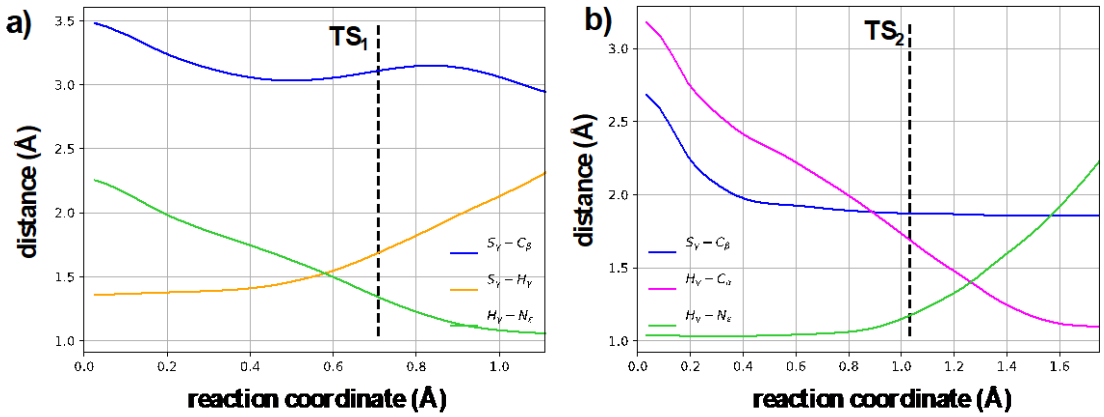


**Figure 4.** Evolution of the selected bond distances along the PMF of the SARS-CoV-2 $M^{pro}$ inhibition with **B3**. a) Formation of the ion pair $\mathbf{E^{(+/-)}}$**:I**. b) Formation of the final **E-I** covalent complex. Vertical dashed lines represent the position of the optimized TS structures.

According to our results, the full reaction mechanism of the inhibition of SARS-CoV-2 $M^{pro}$ cysteine protease by **B3** takes place in two steps. First, the proton from C145 is transferred to H41 with an activation energy barrier of 10.2 ± 0.3 kcal·mol$^{-1}$. The resulting ion pair complex, $\mathbf{E^{(+/-)}}$**:I**, a zwitterion species that according to previous studies is well described by the M06-2X functional here,[49] is clearly less stable than the initial complex in which both residues of the C145/H41 dyad are in their neutral states (by ca. 8 kcal·mol$^{-1}$). This result agrees with our previous computational studies of the proteolysis reaction and the inhibition reaction with different inhibitors.[13,15] Thus, despite the quantitative energetic difference between the ion pair and the neutral form that appears to be dependent on the substrate, the neutral dyad must be considered as the starting state of the reaction catalyzed by $M^{pro}$. As shown in Figure 4a, the proton transfer from C145 to H41 is associated with a slight approach of the sulfur atom of the former to the nucleophilic atom of the substrate (from 3.5 to 2.8 Å). Then, the covalent bond formation between C145 and the $C_\beta$ atom of the substrate takes place concertedly with the proton transfer from the protonated H41 to the $C_\alpha$ atom of the substrate to reach the final **E-I** covalent complex. Interestingly, the barrier for the ion-pair formation is higher than the barrier of the covalent bond formation, if measured from the intermediate $\mathbf{E^{(+/-)}}$**:I**. Nevertheless, because the first step is endergonic, we measured the activation free energy of the second step from the reactants **E:I** complex and, consequently, this is the rate-limiting step of the process with a free energy barrier of 13.5 ± 1.2 kcal·mol$^{-1}$, with breaking and forming bonds in a very asynchronous process (see Figure 4b). The transition state, **TS2**, defined as the maximum of the PMF but also confirmed by optimizing and characterizing a representative structure at M06-2X/6-31+G(d,p)/MM

level (see Figure 5 and Table S6) as a saddle point of order one, is characterized by Sγ-$C_\beta$ bond formation in a very advanced stage of the process (1.89 Å) but a proton transfer in an early stage of the reaction Hγ-$C_\alpha$ distance of ca. 1.70 Å. This concerted character was also confirmed by tracing the IRC down to the ion pair intermediate and the product from the optimized **TS2**, which in fact was used to generate the free energy profile with the FEP method described above. From a technical point of view, it is important to note that both methods, US and FEP, provide the same description of the process with only slight energetic differences, with or without adding the entropic contribution of the QM region (see Figure 3 vs Figure S8 of the Supporting Information). Finally, the analysis of the average interaction energies (electrostatic plus Lennard-Jones) between residues of $M^{pro}$ and each fragment of the inhibitor **B3** computed at the TS2 shows that the pattern of interactions does not significantly change from the one obtained in the **E:I** complex (see Figure 2a vs Figure S9 of the Supporting Information).

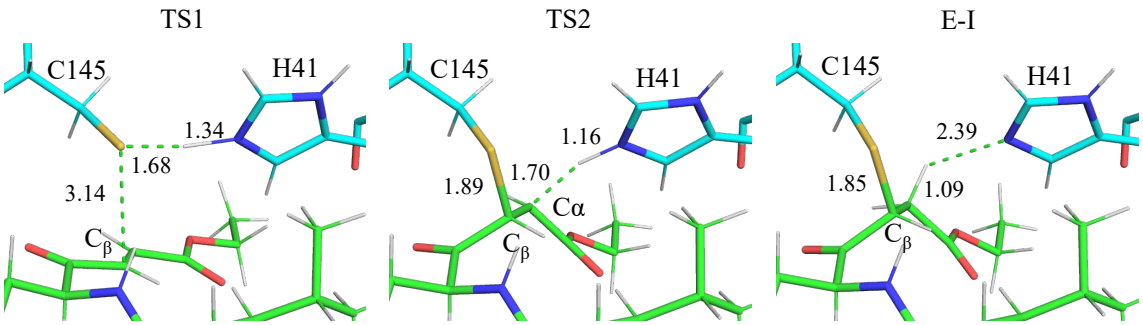


**Figure 5.** Detail of M06-2X/6-31+G(d,p)/MM optimized structures of selected states in the inhibition process of $M^{pro}$ by **B3**. Carbon atoms of the inhibitor are shown in green while those of the catalytic residues C145 and H41 are in cyan. Key distances are in Å.

### Inhibition of SARS-CoV-2 $M^{pro}$ with B4

As shown in Figure 3 and schematically depicted in Scheme 3, the inhibition process with **B4** is equivalent to that obtained with **B3**. Thus, the generation of a transient ion pair intermediate $\mathbf{E^{(+/-)}:I}$ by a proton transfer from C145 to H41 precedes the formation of the covalent complex between C145 and the carbonyl carbon atom of **B4**. The first step is virtually the same as in the case of the inhibition with **B3**, confirming that once again, the neutral reactant complex is favored with respect to the ion pair dyad.[13-18] Evolution of the key distances with the progression of the reaction shows that the proton transfer from C145 to H41 is also associated with an approach of the former to the carbonyl carbon

atom, from 3.0 to 2.2 Å thus generating a more reactive conformation (Figure 6a). Then, the second step, which as in the case of **B3**, represents the rate-limiting step of the full inhibition process, involves the acylation of the protein together with the proton transfer from the protonated H41 to the carbonyl oxygen atom of the inhibitor with an energy barrier, 15.2 ± 1.1 kcal·mol$^{-1}$. This barrier is slightly higher than that obtained for **B3**, 13.5 kcal·mol$^{-1}$. This difference of ~2 kcal·mol$^{-1}$ is also observed in the reaction energies, being the reaction with **B3** slightly more exergonic (–12.5 ± 1.0 kcal·mol$^{-1}$), than the reaction with **B4** (–10.5 ± 0.9 kcal·mol$^{-1}$). A recent computational study of the inhibition mechanism of the cysteine protease rhodesain by a dipeptidyl enoate in our laboratory showed that it can take place through cysteine attack on either the Cβ or the carbonyl carbon atom of the inhibitor, in an exergonic process with a low activation energy barrier.[35] In the current work, as revealed by the evolution of the interatomic distances monitored in Figure 6b, the proton transfer from the positively charged H41 to the carbonyl oxygen atom does not take place directly but through the hydroxyl group of the substrate. Thus, the proton Hγ is transferred from the Nε of H41 to the oxygen atom of the hydroxyl group, O*, simultaneous with the proton transfer, H*, from this hydroxyl oxygen atom to the carbonyl oxygen atom, O, of the substrate. A similar mechanism has been found for the inhibition reaction of M$^{pro}$ with PF-00835231 using similar QM/MM methods but with the B3LYP functional.[18] Our activation free energy is 4.5 kcal·mol$^{-1}$ lower than the one obtained in that study, which could be due to chemical and/or methodological differences. In this regard, limitations of B3LYP for describing thio-Michael additions have been previously noted.[49] It is also worth mentioning that our ion pair intermediate is clearly a stable minimum in the free energy surface, while a metastable ion pair catalytic dyad is formed by the proton transfer from C145 to H41 in that work. The transition state of the second step, defined as the maximum of the PMF and also confirmed by optimizing a representative structure at the M06-2X/6-31+G(d,p)/MM level (see Figure 7 and Table S7) and tracing the IRC down to the ion pair and the final product complex, supports the proposed mechanism. The role played by the terminal hydroxyl group of **B4** in the proton transfer from H41 to the carbonyl oxygen atom of the inhibitor agrees with the results of Hoffman and co-workers, who found a drop of potency in different HMKs when the terminal hydroxyl group was substituted by other groups.[5]

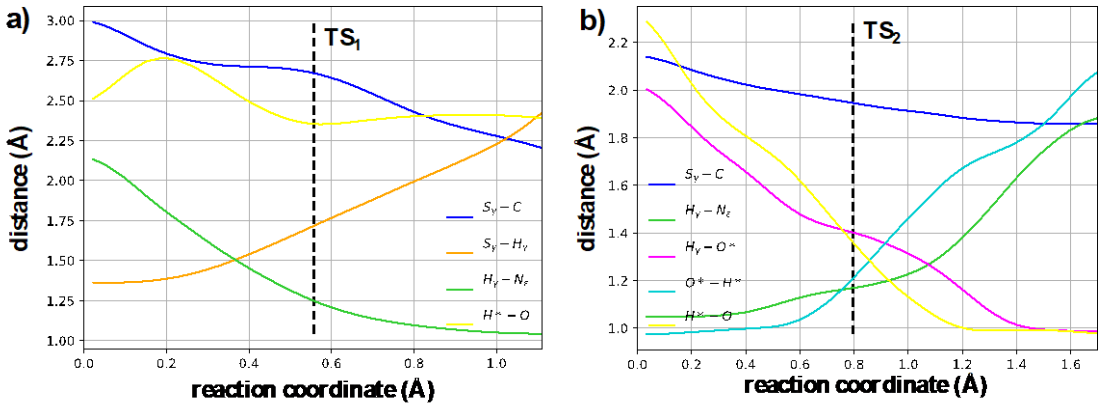


**Figure 6.** Evolution of the selected bond distances along the PMF of the SARS-CoV-2 $M^{pro}$ inhibition by **B4**. a) Formation of the ion pair $\mathbf{E}^{(+/-)}$**:I**. b) Formation of **E-I** covalent complex. Vertical dashed lines represent the position of the optimized TS structures.

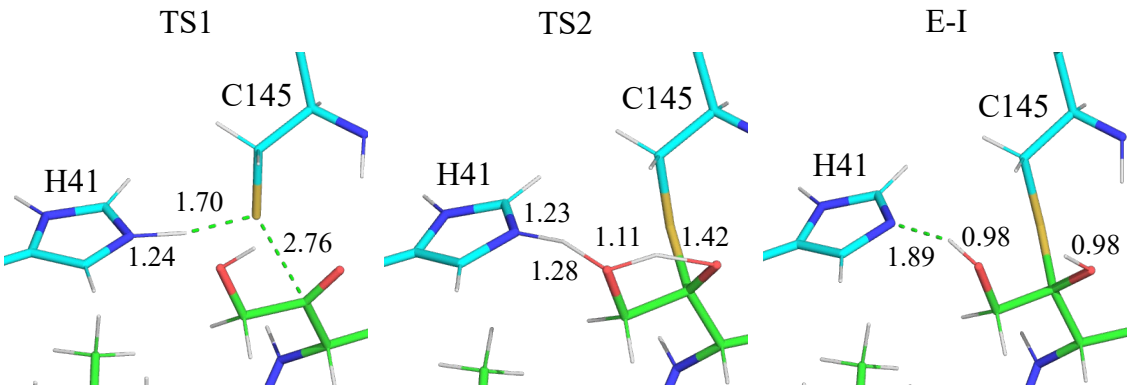


**Figure 7.** Detail of M06-2X/6-31+G(d,p)/MM optimized structures of selected states in the inhibition process of $M^{pro}$ by **B4**. Carbon atoms of the inhibitor are shown in green while those of the catalytic residues C145 and H41 are in cyan. Key distances are in Å.

Finally, as in the case of **B3**, the analysis of the average interaction energies between residues of $M^{pro}$ and each fragment of the inhibitor **B4** computed at the TS2 shows that the pattern of interactions does not significantly change from the one obtained in the **E:I** complex (see Figure 2b vs Figures S10 of the Supporting Information).

## CONCLUSIONS

We report a detailed computational study of the inhibition of SARS-CoV-2 $M^{pro}$ with two proposed covalent (peptidyl) inhibitors: **B3** and **B4**. Both inhibitors share the same recognition part, which is equivalent to that proposed in our previous study,[13] but differ in the activated carbonyl warheads. The results provide information on warhead effects in SARS-CoV-2 $M^{pro}$ covalent inhibitors. The full inhibition processes have been explored with two different DFT/MM methods: first, FEP methods starting from optimized TSs; and second, US relying on the nudged elastic band and the calculation of

the minimum energy paths. There is good agreement between the results derived from these different methodologies.

Our results show that the inhibition process with both compounds takes place by a two-step mechanism, in which the formation of a high energy intermediate (the $C145^{-}/H41^{+}$ ion pair) precedes the protein-inhibitor covalent bond formation. Analysis of the free energy profiles, the geometries of the states appearing along the reaction path, and the interactions between the inhibitors and the different pockets of the active site, confirms a notable impact of the warhead on the kinetics and thermodynamics of the process of the second step. This second step (corresponding to enzyme-inhibitor covalent bond formation) appears to be the rate-limiting step of the process, for both inhibitors, , with an activation free energy of 13.5 ± 1.2 and 15.2 ± 1.1 kcal·mol$^{-1}$ for **B3** and **B4**, respectively. The lower activation free energy of **B3**, together with a slightly more stable final covalent product (by 2 kcal·mol$^{-1}$), suggest that future designs should be based on the modification over this kind of warhead introduced in **B3**. In addition, the highly disfavored reverse processes in both cases (26.0 and 25.7 kcal·mol$^{-1}$ for **B3** and **B4**, respectively) suggest a clear irreversible character of both proposed new compounds, with potential corresponding advantages for medicinal applications

It is important to note that our previously proposed peptidyl nitroalkene inhibitor, **B2**, which shares the same recognition moiety as **B3** and **B4**, showed a slightly lower activation energy barrier (9.8 kcal·mol$^{-1}$) and a less exergonic inhibition process (–11.4 kcal·mol$^{-1}$). These differences may be partially due to the different computational strategies, but it could also be an advantage to obtain more irreversible-character inhibitors. These results are in good agreement with available experimental data on peptidyl covalent $M^{pro}$ inhibitors, but there is no biochemical data for a direct comparison with our proposed compounds.

Analysis of the QM-MM interaction energies between the inhibitor and the residues in the substrate-binding pockets of $M^{pro}$ confirms the predictions assumed during the design of **B3** and **B4,** and the conclusions from analysis of the structures optimized at the DFT/MM level. The interactions between the protein and the inhibitors are dominated by those in the P1:::S1 site, as in our previous studies.[13,15] Finally, the good overlap between the structures of either the reactant complex E:I or the final covalent product E-I and two cocrystal structures of the covalent adduct of similar compounds bound to SARS-CoV-2 $M^{pro}$ suggests that **B3** and **B4** can bind well in the active site. The low barrier obtained for **B4** suggests that the terminal hydroxyl group is an important structural element in its

inhibitory activity. This would also mean that modulation of the p$K_a$ of this group could represent an effective strategy to improve the potency of this specific class of HMKs.

In summary, our QM/MM study of the inhibition of $M^{pro}$ by two covalent (peptidyl) inhibitors, **B3** and **B4**, which we designed based on medicinal chemistry experience and results derived from our previous computational studies, indicates that both, but particularly **B3,** could be used as a template to redesign promising candidates as drug leads against COVID-19. From the drug discovery standpoint, the development of highly selective compounds can benefit from the $M^{pro}$ specificity in cleaving proteins after the Gln residue, a characteristic not observed in human enzymes.

## ASSOCIATED CONTENT

**Electronic supplementary information (ESI) available:**

Force field parameters for inhibitors, pKa values of titratable residues computed in the enzyme, detail of the active site and QM-MM partitioning, M06-2X/6-31+G(d,p)/MM FESs obtained with umbrella sampling and FEP methods, list of average important interatomic distances in crucial states along the reaction paths optimized at M06-2X/MM level, protein-inhibitor non-bonding interaction energies, per residue, imaginary frequencies and Cartesian coordinates of the QM atoms and full structures of the optimized TS structures at M06-2X/6-31+G(d,p)/MM level, and figures of strcutres of inhibitors in **E:I** and **E-I** states overlaid with available related X-ray structures.

## ACKNOWLEDGMENT

This work was supported by the Spanish Ministerio de Ciencia, Innovación y Universidades (Grant PGC2018-094852-B-C21 and PID2019-107098RJ-I00), Generalitat Valenciana (Grant AICO/2019/195 and SEJI/2020/007) and Universitat Jaume I (UJI-A2019-04 and UJI-B2020-03). K.A. thanks Generalitat Valenciana (APOSTD/2020/015) for a postdoctoral contract. The authors thankfully acknowledge the computer resources at Mare Nostrum of Barcelona Supercomputing Center (QSB-2021-1-0007), as well as the local computational resources of the Servei d'Informàtica of Universitat Jaume I. AJM thanks EPSRC for support (CCP-BioSim, grant number EP/M022609/1).

## REFERENCES


(1) Eastman, R. T.; Roth, J. S.; Brimacombe, K. R.; Simeonov, A.; Shen, M.; Patnaik, S.; Hall, M. D. Remdesivir: A Review of Its Discovery and Development Leading to Emergency Use Authorization for Treatment of COVID-19. *ACS Cent Sci* **2020**, *6*, 672-683.

(2) Mengist, H. M.; Fan, X.; Jin, T. Designing of improved drugs for COVID-19: Crystal structure of SARS-CoV-2 main protease Mpro. *Signal Transduction and Targeted Therapy* **2020**, *5*, 67.

(3) Zhu, G.; Zhu, C.; Zhu, Y.; Sun, F. Minireview of progress in the structural study of SARS-CoV-2 proteins. *Current Research in Microbial Sciences* **2020**, *1*, 53-61.

(4) Zhang, L.; Lin, D.; Sun, X.; Curth, U.; Drosten, C.; Sauerhering, L.; Becker, S.; Rox, K.; Hilgenfeld, R. Crystal structure of SARS-CoV-2 main protease provides a basis for design of improved α-ketoamide inhibitors. *Science* **2020**, *368*, 409-412.

(5) Hoffman, R. L.; Kania, R. S.; Brothers, M. A.; Davies, J. F.; Ferre, R. A.; Gajiwala, K. S.; He, M.; Hogan, R. J.; Kozminski, K.; Li, L. Y.; Lockner, J. W.; Lou, J.; Marra, M. T.; Mitchell, L. J.; Murray, B. W.; Nieman, J. A.; Noell, S.; Planken, S. P.; Rowe, T.; Ryan, K.; Smith, G. J.; Solowiej, J. E.; Steppan, C. M.; Taggart, B. Discovery of Ketone-Based Covalent Inhibitors of Coronavirus 3CL Proteases for the Potential Therapeutic Treatment of COVID-19. *J. Med. Chem.* **2020**, *63*, 12725-12747.

(6) Jin, Z.; Du, X.; Xu, Y.; Deng, Y.; Liu, M.; Zhao, Y.; Zhang, B.; Li, X.; Zhang, L.; Peng, C.; Duan, Y.; Yu, J.; Wang, L.; Yang, K.; Liu, F.; Jiang, R.; Yang, X.; You, T.; Liu, X.; Yang, X.; Bai, F.; Liu, H.; Liu, X.; Guddat, L. W.; Xu, W.; Xiao, G.; Qin, C.; Shi, Z.; Jiang, H.; Rao, Z.; Yang, H. Structure of Mpro from SARS-CoV-2 and discovery of its inhibitors. *Nature* **2020**, *582*, 289-293.

(7) von Delft, F.; Calmiano, M.; Chodera, J.; Griffen, E.; Lee, A.; London, N.; Matviuk, T.; Perry, B.; Robinson, M.; von Delft, A. A white-knuckle ride of open COVID drug discovery. *Nature* **2021**, *594*, 330-332.

(8) Dai, W.; Zhang, B.; Jiang, X.-M.; Su, H.; Li, J.; Zhao, Y.; Xie, X.; Jin, Z.; Peng, J.; Liu, F.; Li, C.; Li, Y.; Bai, F.; Wang, H.; Cheng, X.; Cen, X.; Hu, S.; Yang, X.; Wang, J.; Liu, X.; Xiao, G.; Jiang, H.; Rao, Z.; Zhang, L.-K.; Xu, Y.; Yang, H.; Liu, H. Structure-based design of antiviral drug candidates targeting the SARS-CoV-2 main protease. *Science* **2020**, *368*, 1331-1335.

(9) Muratov, E. N.; Amaro, R.; Andrade, C. H.; Brown, N.; Ekins, S.; Fourches, D.; Isayev, O.; Kozakov, D.; Medina-Franco, J. L.; Merz, K. M.; Oprea, T. I.; Poroikov, V.; Schneider, G.; Todd, M. H.; Varnek, A.; Winkler, D. A.; Zakharov, A. V.; Cherkasov, A.; Tropsha, A. A critical overview of computational approaches employed for COVID-19 drug discovery. *Chem. Soc. Rev.* **2021**, *50*, 9121-9151.

(10) Deshmukh, M. G.; Ippolito, J. A.; Zhang, C.-H.; Stone, E. A.; Reilly, R. A.; Miller, S. J.; Jorgensen, W. L.; Anderson, K. S. Structure-guided design of a perampanel-derived pharmacophore targeting the SARS-CoV-2 main protease. *Structure* **2021**, *29*, 823-833.e825.

(11) Zhang, C.-H.; Spasov, K. A.; Reilly, R. A.; Hollander, K.; Stone, E. A.; Ippolito, J. A.; Liosi, M.-E.; Deshmukh, M. G.; Tirado-Rives, J.; Zhang, S.; Liang, Z.; Miller, S. J.; Isaacs, F.; Lindenbach, B. D.; Anderson, K. S.; Jorgensen, W. L. Optimization of Triarylpyridinone Inhibitors of the Main Protease of SARS-CoV-

2 to Low-Nanomolar Antiviral Potency. *ACS Med. Chem. Lett.* **2021**, *12*, 1325-1332.

(12) Zhang, C.-H.; Stone, E. A.; Deshmukh, M.; Ippolito, J. A.; Ghahremanpour, M. M.; Tirado-Rives, J.; Spasov, K. A.; Zhang, S.; Takeo, Y.; Kudalkar, S. N.; Liang, Z.; Isaacs, F.; Lindenbach, B.; Miller, S. J.; Anderson, K. S.; Jorgensen, W. L. Potent Noncovalent Inhibitors of the Main Protease of SARS-CoV-2 from Molecular Sculpting of the Drug Perampanel Guided by Free Energy Perturbation Calculations. *ACS Central Science* **2021**, *7*, 467-475.

(13) Arafet, K.; Serrano-Aparicio, N.; Lodola, A.; Mulholland, A. J.; González, F. V.; Świderek, K.; Moliner, V. Mechanism of inhibition of SARS-CoV-2 Mpro by N3 peptidyl Michael acceptor explained by QM/MM simulations and design of new derivatives with tunable chemical reactivity. *Chem. Sci.* **2021**, *12*, 1433-1444.

(14) Ramos-Guzmán, C. A.; Ruiz-Pernía, J. J.; Tuñón, I. Unraveling the SARS-CoV-2 Main Protease Mechanism Using Multiscale Methods. *ACS Catalysis* **2020**, *10*, 12544-12554.

(15) Świderek, K.; Moliner, V. Revealing the Molecular Mechanisms of Proteolysis of SARS-CoV-2 Mpro from QM/MM Computational Methods. *Chem. Sci.* **2020**, *11*, 10626-10630.

(16) Chan, H. T. H.; Moesser, M. A.; Walters, R. K.; Malla, T. R.; Twidale, R. M.; John, T.; Deeks, H. M.; Johnston-Wood, T.; Mikhailov, V.; Sessions, R. B.; Dawson, W.; Salah, E.; Lukacik, P.; Strain-Damerell, C.; Owen, C. D.; Nakajima, T.; Świderek, K.; Lodola, A.; Moliner, V.; Glowacki, D. R.; Walsh, M. A.; Schofield, C. J.; Genovese, L.; Shoemark, D. K.; Mulholland, A. J.; Duarte, F.; Morris, G. M. *Chem. Sci.* **2021**, DOI: 10.1039/D1SC03628A.

(17) Pavlova, A.; Lynch, D. L.; Daidone, I.; Zanetti-Polzi, L.; Smith, M. D.; Chipot, C.; Kneller, D. W.; Kovalevsky, A.; Coates, L.; Golosov, A. A.; Dickson, C. J.; Velez-Vega, C.; Duca, J. S.; Vermaas, J. V.; Pang, Y. T.; Acharya, A.; Parks, J. M.; Smith, J. C.; Gumbart, J. C. Inhibitor binding influences the protonation states of histidines in SARS-CoV-2 main protease. *Chem. Sci.* **2021**, *12*, 1513-1527.

(18) Ramos-Guzmán, C. A.; Ruiz-Pernía, J. J.; Tunón, I. *Angew. Chem. Int. Ed.* **2021**, DOI: https://doi.org/10.1002/anie.202110027.

(19) Kneller, D. W.; Phillips, G.; Weiss, K. L.; Pant, S.; Zhang, Q.; O'Neill, H. M.; Coates, L.; Kovalevsky, A. Unusual zwitterionic catalytic site of SARS-CoV-2 main protease revealed by neutron crystallography. *J. Biol. Chem.* **2020**, *295*, 17365-17373.

(20) Lodola, A.; Callegari, D.; Scalvini, L.; Rivara, S.; Mor, M. Design and SAR Analysis of Covalent Inhibitors Driven by Hybrid QM/MM Simulations. *Methods Mol Biol* **2020**, *2114*, 307-337.

(21) Kastrati, I.; Siklos, M. I.; Calderon-Gierszal, E. L.; El-Shennawy, L.; Georgieva, G.; Thayer, E. N.; Thatcher, G. R. J.; Frasor, J. Dimethyl Fumarate Inhibits the Nuclear Factor κB Pathway in Breast Cancer Cells by Covalent Modification of p65 Protein*. *J. Biol. Chem.* **2016**, *291*, 3639-3647.

(22) Rosa, A. C.; Benetti, E.; Gallicchio, M.; Boscaro, V.; Cangemi, L.; Dianzani, C.; Miglio, G. Analyzing Cysteine Site Neighbors in Proteins to Reveal Dimethyl Fumarate Targets. *Proteomics* **2019**, *19*, 1800301.

(23) Wang, J.; Wang, W.; Kollman, P. A.; Case, D. A. Automatic atom type and bond type perception in molecular mechanical calculations. *Journal of Molecular Graphics & Modelling* **2006**, *25*, 247-260.

(24) Olsson, M. H. M.; Sondergaard, C. R.; Rostkowski, M.; Jensen, J. H. PROPKA3: Consistent Treatment of Internal and Surface Residues in Empirical pKa Predictions. *J. Chem. Theory Comput.* **2011**, *7*, 525-537.
(25) Jorgensen, W. L.; Chandrasekhar, J.; Madura, J. D.; Impey, R. W.; Klein, M. L. Comparison of simple potential functions for simulating liquid water. *J. Chem. Phys.* **1983**, *79*, 926-935.
(26) Duan, Y.; Wu, C.; Chowdhury, S.; Lee, M. C.; Xiong, G. M.; Zhang, W.; Yang, R.; Cieplak, P.; Luo, R.; Lee, T.; Caldwell, J.; Wang, J. M.; Kollman, P. A point-charge force field for molecular mechanics simulations of proteins based on condensed-phase quantum mechanical calculations. *J. Comput. Chem.* **2003**, *24*, 1999-2012.
(27) Phillips, J. C.; Braun, R.; Wang, W.; Gumbart, J.; Tajkhorshid, E.; Villa, E.; Chipot, C.; Skeel, R. D.; Kalé, L.; Schulten, K. Scalable molecular dynamics with NAMD. *J. Comput. Chem.* **2005**, *26*, 1781-1802.
(28) Grest, G. S.; Kremer, K. Molecular dynamics simulation for polymers in the presence of a heat bath. *Phys. Rev. A* **1986**, *33*, 3628-3631.
(29) Roe, D. R.; Cheatham, T. E. PTRAJ and CPPTRAJ: Software for Processing and Analysis of Molecular Dynamics Trajectory Data. *J. Chem. Theory Comput.* **2013**, *9*, 3084-3095.
(30) Martí, S. QMCube (QM3): An all-purpose suite for multiscale QM/MM calculations. *J. Comput. Chem.* **2021**, *42*, 447-457.
(31) M. J. Frisch; G. W. Trucks; H. B. Schlegel; G. E. Scuseria; M. A. Robb; J. R. Cheeseman; G. Scalmani; V. Barone; B. Mennucci; G. A. Petersson; H. Nakatsuji; M. Caricato, X. L., H. P. Hratchian, A. F. Izmaylov, J. Bloino, G. Zheng, J. L. Sonnenberg, M. Hada, M. Ehara, K. Toyota, R. Fukuda, J. Hasegawa, M. Ishida, T. Nakajima, Y. Honda, O. Kitao, H. Nakai, T. Vreven, J. A. Montgomery, Jr., J. E. Peralta, F. Ogliaro, M. Bearpark, J. J. Heyd, E. Brothers, K. N. Kudin, V. N. Staroverov, R. Kobayashi, J. Normand, K. Raghavachari, A. Rendell, J. C. Burant, S. S. Iyengar, J. Tomasi, M. Cossi, N. Rega, J. M. Millam, M. Klene, J. E. Knox, J. B. Cross, V. Bakken, C. Adamo, J. Jaramillo, R. Gomperts, R. E. Stratmann, O. Yazyev, A. J. Austin, R. Cammi, C. Pomelli, J. W. Ochterski, R. L. Martin, K. Morokuma, V. G. Zakrzewski, G. A. Voth, P. Salvador, J. J. Dannenberg, S. Dapprich, A. D. Daniels, Ö. Farkas, J. B. Foresman, J. V. Ortiz, J. Cioslowski, D. J. Fox, Wallingford, CT, **2009**.
(32) Zhao, Y.; Truhlar, D. G. The M06 suite of density functionals for main group thermochemistry, thermochemical kinetics, noncovalent interactions, excited states, and transition elements: two new functionals and systematic testing of four M06-class functionals and 12 other functionals. *Theor. Chem. Acc.* **2008**, *120*, 215-241.
(33) Hehre, W. J.; Radom, L.; Schleyer, P. V. R.; Pople, J. A., *Ab Initio Molecular Orbital Theory*, John Wiley, New York, **1986**.
(34) Arafet, K.; Ferrer, S.; Moliner, V. Computational Study of the Catalytic Mechanism of the Cruzain Cysteine Protease. *ACS Catalysis* **2017**, *7*, 1207-1215.
(35) Arafet, K.; González, F. V.; Moliner, V. Elucidating the Dual Mode of Action of Dipeptidyl Enoates in the Inhibition of Rhodesain Cysteine Proteases. *Chemistry – A European Journal* **2021**, *27*, 10142-10150.
(36) Henkelman, G.; Jónsson, H. Improved tangent estimate in the nudged elastic band method for finding minimum energy paths and saddle points. *The Journal of Chemical Physics* **2000**, *113*, 9978-9985.

(37) Turner, A. J.; Moliner, V.; Williams, I. H. Transition-state structural refinement with GRACE and CHARMM: Flexible QM/MM modelling for lactate dehydrogenase. *Phys. Chem. Chem. Phys.* **1999**, *1*, 1323-1331.
(38) Martí, S.; Moliner, V.; Tuñón, I. Improving the QM/MM description of chemical processes: A dual level strategy to explore the potential energy surface in very large systems. *J. Chem. Theory Comput.* **2005**, *1*, 1008-1016.
(39) Swiderek, K.; Tuñón, I.; Martí, S.; Moliner, V.; Bertran, J. Role of Solvent on Nonenzymatic Peptide Bond Formation Mechanisms and Kinetic Isotope Effects. *J. Am. Chem. Soc.* **2013**, *135*, 8708-8719.
(40) Swiderek, K.; Marti, S.; Tunon, I.; Moliner, V.; Bertran, J. Peptide Bond Formation Mechanism Catalyzed by Ribosome. *J. Am. Chem. Soc.* **2015**, *137*, 12024-12034.
(41) Krzemińska, A.; Świderek, K. Molecular Insights into the Substrate-Assisted Mechanism of Viral DNA 3′-End Processing in Intasome of Prototype Foamy Virus Integrase from Molecular Dynamic and QM/MM Studies. *J. Chem. Inf. Model.* **2019**, *59*, 2995-3005.
(42) Galmés, M. A.; Świderek, K.; Moliner, V. Computational Studies Suggest Promiscuous Candida antarctica Lipase B as an Environmentally Friendly Alternative for the Production of Epoxides. *J. Chem. Inf. Model.* **2021**, *61*, 3604-3614.
(43) Breneman, C. M.; Wiberg, K. B. Determining atom-centered monopoles from molecular electrostatic potentials. The need for high sampling density in formamide conformational analysis. *J. Comput. Chem.* **1990**, *11*, 361-373.
(44) Torrie, G. M.; Valleau, J. P. Non-physical sampling distributions in Monte_Carlo Free-Energy estimation-Umbrella Sampling. *J. Comput. Phys.* **1977**, *23*, 187-199.
(45) Kumar, S.; Bouzida, D.; Swendsen, R. H.; Kollman, P. A.; Rosenberg, J. M. The Weighted Histogram Analysis Method for Free-Energy calculations on Biomolecules.1. The Method. *J. Comput. Chem.* **1992**, *13*, 1011-1021.
(46) Zinovjev, K.; Tuñón, I. Reaction coordinates and transition states in enzymatic catalysis. *WIREs Computational Molecular Science* **2018**, *8*, e1329.
(47) Hub, J. S.; de Groot, B. L.; van der Spoel, D. g_wham—A Free Weighted Histogram Analysis Implementation Including Robust Error and Autocorrelation Estimates. *J. Chem. Theory Comput.* **2010**, *6*, 3713-3720.
(48) Dewar, M. J. S.; Zoebisch, E. G.; Healy, E. F.; Stewart, J. J. P. The development and use of quantum mechanical molecular-models. 76. AM1: A new general purpose quantum mechanical molecular model. *J. Am. Chem. Soc.* **1985**, *107*, 3902-3909.
(49) Smith, J. M.; Jami Alahmadi, Y.; Rowley, C. N. Range-Separated DFT Functionals are Necessary to Model Thio-Michael Additions. *J. Chem. Theory Comput.* **2013**, *9*, 4860-4865.

(1) Eastman, R. T.; Roth, J. S.; Brimacombe, K. R.; Simeonov, A.; Shen, M.; Patnaik, S.; Hall, M. D. Remdesivir: A Review of Its Discovery and Development Leading to Emergency Use Authorization for Treatment of COVID-19. *ACS Cent Sci* **2020**, *6*, 672-683.

(2) Mengist, H. M.; Fan, X.; Jin, T. Designing of improved drugs for COVID-19: Crystal structure of SARS-CoV-2 main protease Mpro. *Signal Transduction and Targeted Therapy* **2020**, *5*, 67.

(3) Zhu, G.; Zhu, C.; Zhu, Y.; Sun, F. Minireview of progress in the structural study of SARS-CoV-2 proteins. *Current Research in Microbial Sciences* **2020**, *1*, 53-61.

(4) Zhang, L.; Lin, D.; Sun, X.; Curth, U.; Drosten, C.; Sauerhering, L.; Becker, S.; Rox, K.; Hilgenfeld, R. Crystal structure of SARS-CoV-2 main protease provides a basis for design of improved α-ketoamide inhibitors. *Science* **2020**, *368*, 409-412.

(5) Hoffman, R. L.; Kania, R. S.; Brothers, M. A.; Davies, J. F.; Ferre, R. A.; Gajiwala, K. S.; He, M.; Hogan, R. J.; Kozminski, K.; Li, L. Y.; Lockner, J. W.; Lou, J.; Marra, M. T.; Mitchell, L. J.; Murray, B. W.; Nieman, J. A.; Noell, S.; Planken, S. P.; Rowe, T.; Ryan, K.; Smith, G. J.; Solowiej, J. E.; Steppan, C. M.; Taggart, B. Discovery of Ketone-Based Covalent Inhibitors of Coronavirus 3CL Proteases for the Potential Therapeutic Treatment of COVID-19. *J. Med. Chem.* **2020**, *63*, 12725-12747.

(6) Jin, Z.; Du, X.; Xu, Y.; Deng, Y.; Liu, M.; Zhao, Y.; Zhang, B.; Li, X.; Zhang, L.; Peng, C.; Duan, Y.; Yu, J.; Wang, L.; Yang, K.; Liu, F.; Jiang, R.; Yang, X.; You, T.; Liu, X.; Yang, X.; Bai, F.; Liu, H.; Liu, X.; Guddat, L. W.; Xu, W.; Xiao, G.; Qin, C.; Shi, Z.; Jiang, H.; Rao, Z.; Yang, H. Structure of Mpro from SARS-CoV-2 and discovery of its inhibitors. *Nature* **2020**, *582*, 289-293.

(7) von Delft, F.; Calmiano, M.; Chodera, J.; Griffen, E.; Lee, A.; London, N.; Matviuk, T.; Perry, B.; Robinson, M.; von Delft, A. A white-knuckle ride of open COVID drug discovery. *Nature* **2021**, *594*, 330-332.

(8) Dai, W.; Zhang, B.; Jiang, X.-M.; Su, H.; Li, J.; Zhao, Y.; Xie, X.; Jin, Z.; Peng, J.; Liu, F.; Li, C.; Li, Y.; Bai, F.; Wang, H.; Cheng, X.; Cen, X.; Hu, S.; Yang, X.; Wang, J.; Liu, X.; Xiao, G.; Jiang, H.; Rao, Z.; Zhang, L.-K.; Xu, Y.; Yang, H.; Liu, H. Structure-based design of antiviral drug candidates targeting the SARS-CoV-2 main protease. *Science* **2020**, *368*, 1331-1335.

(9) Muratov, E. N.; Amaro, R.; Andrade, C. H.; Brown, N.; Ekins, S.; Fourches, D.; Isayev, O.; Kozakov, D.; Medina-Franco, J. L.; Merz, K. M.; Oprea, T. I.; Poroikov, V.; Schneider, G.; Todd, M. H.; Varnek, A.; Winkler, D. A.; Zakharov, A. V.; Cherkasov, A.; Tropsha, A. A critical overview of computational approaches employed for COVID-19 drug discovery. *Chem. Soc. Rev.* **2021**, *50*, 9121-9151.

(10) Deshmukh, M. G.; Ippolito, J. A.; Zhang, C.-H.; Stone, E. A.; Reilly, R. A.; Miller, S. J.; Jorgensen, W. L.; Anderson, K. S. Structure-guided design of a perampanel-derived pharmacophore targeting the SARS-CoV-2 main protease. *Structure* **2021**, *29*, 823-833.e825.

(11) Zhang, C.-H.; Spasov, K. A.; Reilly, R. A.; Hollander, K.; Stone, E. A.; Ippolito, J. A.; Liosi, M.-E.; Deshmukh, M. G.; Tirado-Rives, J.; Zhang, S.; Liang, Z.; Miller, S. J.; Isaacs, F.; Lindenbach, B. D.; Anderson, K. S.; Jorgensen, W. L. Optimization of Triarylpyridinone Inhibitors of the Main Protease of SARS-CoV-2 to Low-Nanomolar Antiviral Potency. *ACS Med. Chem. Lett.* **2021**, *12*, 1325-1332.

(12) Zhang, C.-H.; Stone, E. A.; Deshmukh, M.; Ippolito, J. A.; Ghahremanpour, M. M.; Tirado-Rives, J.; Spasov, K. A.; Zhang, S.; Takeo, Y.; Kudalkar, S. N.; Liang, Z.; Isaacs, F.; Lindenbach, B.; Miller, S. J.; Anderson, K. S.; Jorgensen, W. L. Potent Noncovalent Inhibitors of the Main Protease of SARS-CoV-2 from Molecular Sculpting of the Drug Perampanel Guided by Free Energy Perturbation Calculations. *ACS Central Science* **2021**, *7*, 467-475.

(13) Arafet, K.; Serrano-Aparicio, N.; Lodola, A.; Mulholland, A. J.; González, F. V.; Świderek, K.; Moliner, V. Mechanism of inhibition of SARS-CoV-2 Mpro by N3 peptidyl Michael acceptor explained by QM/MM simulations and design of new derivatives with tunable chemical reactivity. *Chem. Sci.* **2021**, *12*, 1433-1444.

(14) Ramos-Guzmán, C. A.; Ruiz-Pernía, J. J.; Tuñón, I. Unraveling the SARS-CoV-2 Main Protease Mechanism Using Multiscale Methods. *ACS Catalysis* **2020**, *10*, 12544-12554.

(15) Świderek, K.; Moliner, V. Revealing the Molecular Mechanisms of Proteolysis of SARS-CoV-2 Mpro from QM/MM Computational Methods. *Chem. Sci.* **2020**, *11*, 10626-10630.

(16) Chan, H. T. H.; Moesser, M. A.; Walters, R. K.; Malla, T. R.; Twidale, R. M.; John, T.; Deeks, H. M.; Johnston-Wood, T.; Mikhailov, V.; Sessions, R. B.; Dawson, W.; Salah, E.; Lukacik, P.; Strain-Damerell, C.; Owen, C. D.; Nakajima, T.; Świderek, K.; Lodola, A.; Moliner, V.; Glowacki, D. R.; Walsh, M. A.; Schofield, C. J.; Genovese, L.; Shoemark, D. K.; Mulholland, A. J.; Duarte, F.; Morris, G. M. *Chem. Sci.* **2021**, DOI: 10.1039/D1SC03628A.

(17) Pavlova, A.; Lynch, D. L.; Daidone, I.; Zanetti-Polzi, L.; Smith, M. D.; Chipot, C.; Kneller, D. W.; Kovalevsky, A.; Coates, L.; Golosov, A. A.; Dickson, C. J.; Velez-Vega, C.; Duca, J. S.; Vermaas, J. V.; Pang, Y. T.; Acharya, A.; Parks, J. M.; Smith, J. C.; Gumbart, J. C. Inhibitor binding influences the protonation states of histidines in SARS-CoV-2 main protease. *Chem. Sci.* **2021**, *12*, 1513-1527.

(18) Ramos-Guzmán, C. A.; Ruiz-Pernía, J. J.; Tunón, I. *Angew. Chem. Int. Ed.* **2021**, DOI: https://doi.org/10.1002/anie.202110027.

(19) Kneller, D. W.; Phillips, G.; Weiss, K. L.; Pant, S.; Zhang, Q.; O'Neill, H. M.; Coates, L.; Kovalevsky, A. Unusual zwitterionic catalytic site of SARS-CoV-2 main protease revealed by neutron crystallography. *J. Biol. Chem.* **2020**, *295*, 17365-17373.

(20) Lodola, A.; Callegari, D.; Scalvini, L.; Rivara, S.; Mor, M. Design and SAR Analysis of Covalent Inhibitors Driven by Hybrid QM/MM Simulations. *Methods Mol Biol* **2020**, *2114*, 307-337.

(21) Kastrati, I.; Siklos, M. I.; Calderon-Gierszal, E. L.; El-Shennawy, L.; Georgieva, G.; Thayer, E. N.; Thatcher, G. R. J.; Frasor, J. Dimethyl Fumarate Inhibits the Nuclear Factor κB Pathway in Breast Cancer Cells by Covalent Modification of p65 Protein*. *J. Biol. Chem.* **2016**, *291*, 3639-3647.

(22) Rosa, A. C.; Benetti, E.; Gallicchio, M.; Boscaro, V.; Cangemi, L.; Dianzani, C.; Miglio, G. Analyzing Cysteine Site Neighbors in Proteins to Reveal Dimethyl Fumarate Targets. *Proteomics* **2019**, *19*, 1800301.

(23) Wang, J.; Wang, W.; Kollman, P. A.; Case, D. A. Automatic atom type and bond type perception in molecular mechanical calculations. *Journal of Molecular Graphics & Modelling* **2006**, *25*, 247-260.

(24) Olsson, M. H. M.; Sondergaard, C. R.; Rostkowski, M.; Jensen, J. H. PROPKA3: Consistent Treatment of Internal and Surface Residues in Empirical pKa Predictions. *J. Chem. Theory Comput.* **2011**, *7*, 525-537.

(25) Jorgensen, W. L.; Chandrasekhar, J.; Madura, J. D.; Impey, R. W.; Klein, M. L. Comparison of simple potential functions for simulating liquid water. *J. Chem. Phys.* **1983**, *79*, 926-935.
(26) Duan, Y.; Wu, C.; Chowdhury, S.; Lee, M. C.; Xiong, G. M.; Zhang, W.; Yang, R.; Cieplak, P.; Luo, R.; Lee, T.; Caldwell, J.; Wang, J. M.; Kollman, P. A point-charge force field for molecular mechanics simulations of proteins based on condensed-phase quantum mechanical calculations. *J. Comput. Chem.* **2003**, *24*, 1999-2012.
(27) Phillips, J. C.; Braun, R.; Wang, W.; Gumbart, J.; Tajkhorshid, E.; Villa, E.; Chipot, C.; Skeel, R. D.; Kalé, L.; Schulten, K. Scalable molecular dynamics with NAMD. *J. Comput. Chem.* **2005**, *26*, 1781-1802.
(28) Grest, G. S.; Kremer, K. Molecular dynamics simulation for polymers in the presence of a heat bath. *Phys. Rev. A* **1986**, *33*, 3628-3631.
(29) Roe, D. R.; Cheatham, T. E. PTRAJ and CPPTRAJ: Software for Processing and Analysis of Molecular Dynamics Trajectory Data. *J. Chem. Theory Comput.* **2013**, *9*, 3084-3095.
(30) Martí, S. QMCube (QM3): An all-purpose suite for multiscale QM/MM calculations. *J. Comput. Chem.* **2021**, *42*, 447-457.
(31) M. J. Frisch; G. W. Trucks; H. B. Schlegel; G. E. Scuseria; M. A. Robb; J. R. Cheeseman; G. Scalmani; V. Barone; B. Mennucci; G. A. Petersson; H. Nakatsuji; M. Caricato, X. L., H. P. Hratchian, A. F. Izmaylov, J. Bloino, G. Zheng, J. L. Sonnenberg, M. Hada, M. Ehara, K. Toyota, R. Fukuda, J. Hasegawa, M. Ishida, T. Nakajima, Y. Honda, O. Kitao, H. Nakai, T. Vreven, J. A. Montgomery, Jr., J. E. Peralta, F. Ogliaro, M. Bearpark, J. J. Heyd, E. Brothers, K. N. Kudin, V. N. Staroverov, R. Kobayashi, J. Normand, K. Raghavachari, A. Rendell, J. C. Burant, S. S. Iyengar, J. Tomasi, M. Cossi, N. Rega, J. M. Millam, M. Klene, J. E. Knox, J. B. Cross, V. Bakken, C. Adamo, J. Jaramillo, R. Gomperts, R. E. Stratmann, O. Yazyev, A. J. Austin, R. Cammi, C. Pomelli, J. W. Ochterski, R. L. Martin, K. Morokuma, V. G. Zakrzewski, G. A. Voth, P. Salvador, J. J. Dannenberg, S. Dapprich, A. D. Daniels, Ö. Farkas, J. B. Foresman, J. V. Ortiz, J. Cioslowski, D. J. Fox, Wallingford, CT, **2009**.
(32) Zhao, Y.; Truhlar, D. G. The M06 suite of density functionals for main group thermochemistry, thermochemical kinetics, noncovalent interactions, excited states, and transition elements: two new functionals and systematic testing of four M06-class functionals and 12 other functionals. *Theor. Chem. Acc.* **2008**, *120*, 215-241.
(33) Hehre, W. J.; Radom, L.; Schleyer, P. V. R.; Pople, J. A., *Ab Initio Molecular Orbital Theory*, John Wiley, New York, **1986**.
(34) Arafet, K.; Ferrer, S.; Moliner, V. Computational Study of the Catalytic Mechanism of the Cruzain Cysteine Protease. *ACS Catalysis* **2017**, *7*, 1207-1215.
(35) Arafet, K.; González, F. V.; Moliner, V. Elucidating the Dual Mode of Action of Dipeptidyl Enoates in the Inhibition of Rhodesain Cysteine Proteases. *Chemistry – A European Journal* **2021**, *27*, 10142-10150.
(36) Henkelman, G.; Jónsson, H. Improved tangent estimate in the nudged elastic band method for finding minimum energy paths and saddle points. *The Journal of Chemical Physics* **2000**, *113*, 9978-9985.
(37) Turner, A. J.; Moliner, V.; Williams, I. H. Transition-state structural refinement with GRACE and CHARMM: Flexible QM/MM modelling for lactate dehydrogenase. *Phys. Chem. Chem. Phys.* **1999**, *1*, 1323-1331.

(38) Martí, S.; Moliner, V.; Tuñón, I. Improving the QM/MM description of chemical processes: A dual level strategy to explore the potential energy surface in very large systems. *J. Chem. Theory Comput.* **2005**, *1*, 1008-1016.
(39) Swiderek, K.; Tuñón, I.; Martí, S.; Moliner, V.; Bertran, J. Role of Solvent on Nonenzymatic Peptide Bond Formation Mechanisms and Kinetic Isotope Effects. *J. Am. Chem. Soc.* **2013**, *135*, 8708-8719.
(40) Swiderek, K.; Marti, S.; Tunon, I.; Moliner, V.; Bertran, J. Peptide Bond Formation Mechanism Catalyzed by Ribosome. *J. Am. Chem. Soc.* **2015**, *137*, 12024-12034.
(41) Krzemińska, A.; Świderek, K. Molecular Insights into the Substrate-Assisted Mechanism of Viral DNA 3′-End Processing in Intasome of Prototype Foamy Virus Integrase from Molecular Dynamic and QM/MM Studies. *J. Chem. Inf. Model.* **2019**, *59*, 2995-3005.
(42) Galmés, M. A.; Świderek, K.; Moliner, V. Computational Studies Suggest Promiscuous Candida antarctica Lipase B as an Environmentally Friendly Alternative for the Production of Epoxides. *J. Chem. Inf. Model.* **2021**, *61*, 3604-3614.
(43) Breneman, C. M.; Wiberg, K. B. Determining atom-centered monopoles from molecular electrostatic potentials. The need for high sampling density in formamide conformational analysis. *J. Comput. Chem.* **1990**, *11*, 361-373.
(44) Torrie, G. M.; Valleau, J. P. Non-physical sampling distributions in Monte_Carlo Free-Energy estimation-Umbrella Sampling. *J. Comput. Phys.* **1977**, *23*, 187-199.
(45) Kumar, S.; Bouzida, D.; Swendsen, R. H.; Kollman, P. A.; Rosenberg, J. M. The Weighted Histogram Analysis Method for Free-Energy calculations on Biomolecules.1. The Method. *J. Comput. Chem.* **1992**, *13*, 1011-1021.
(46) Zinovjev, K.; Tuñón, I. Reaction coordinates and transition states in enzymatic catalysis. *WIREs Computational Molecular Science* **2018**, *8*, e1329.
(47) Hub, J. S.; de Groot, B. L.; van der Spoel, D. g_wham—A Free Weighted Histogram Analysis Implementation Including Robust Error and Autocorrelation Estimates. *J. Chem. Theory Comput.* **2010**, *6*, 3713-3720.
(48) Dewar, M. J. S.; Zoebisch, E. G.; Healy, E. F.; Stewart, J. J. P. The development and use of quantum mechanical molecular-models. 76. AM1: A new general purpose quantum mechanical molecular model. *J. Am. Chem. Soc.* **1985**, *107*, 3902-3909.
(49) Smith, J. M.; Jami Alahmadi, Y.; Rowley, C. N. Range-Separated DFT Functionals are Necessary to Model Thio-Michael Additions. *J. Chem. Theory Comput.* **2013**, *9*, 4860-4865.

Table of Contents Graphic